Large-scale filaments and the intergalactic medium

Kooistra, Robin Rinze

Chapter 5

Faint HI emission in filaments with Apertif

– Robin Kooistra, Marta B. Silva & Saleem Zaroubi –
in prep.

"Luminous beings are we... not this crude matter."

Master Yoda, 3 A.B.Y

Abstract

The connection between large-scale filaments and the galaxies that they house is an essential aspect of galaxy formation and evolution. The upcoming medium deep HI survey with Apertif will allow for a study of a large enough volume to gather statistical properties of these filaments at low redshift. We make a comparison of the ability of Apertif to trace the cosmic web to that of the Sloan Digital Sky survey (SDSS) and categorize the properties of the filaments and the galaxies that surround them. We adopt the 100 Mpc^3 volume EAGLE hydrodynamic cosmological simulation to obtain realistic filaments and estimate the properties of the galaxies. With this simulation, we were able to create a sample of galaxies based on the sensitivity of each survey. This allows us to infer and extract filament spines at $z = 0.05$. We find that an optical survey, in this case SDSS, traces the same major structures of the cosmic web as well as an HI survey with Apertif would. Our conclusions are limited by the use of a simulation instead of observational data, but we find no significant difference between the distributions of the properties of the filaments. Apertif-based filaments are able to trace more blue and thus younger galaxies. Furthermore, Apertif is able to trace almost twice as many filaments longer than 5 h^{-1} Mpc and its galaxy survey is therefore the most ideal of the two for tracing most of the large-scale structures in a survey. We also estimate the total HI mass contained in the galaxies surrounding a filament spine that lie between the 4σ and 1σ detection thresholds of the Apertif medium deep survey. On average, this yields an HI mass of $\sim 10^9 M_\odot$ that would normally not be identified in a galaxy survey due to the 4σ detection requirement, but is still present within the data.

5.1 Introduction

Large galaxy surveys provide a treasure trove for studying the large-scale structure in the Universe. Both the three-dimensional distribution of galaxies and the neutral hydrogen (HI) within galaxies and the intergalactic medium (IGM) are essential for understanding how large-scale filaments can feed galaxies with gas and affect their formation and evolution. Filamentary structure clearly stand out in galaxy redshift surveys, such as the Sloan Digital Sky Survey (SDSS, York et al. 2000; Aihara et al. 2011), the 2-degree Field (2dF) Galaxy Redshift Survey (Colless 1999) and the Two Micron All-Sky Redshift Survey (2MRS; Huchra et al. 2012) and their distributions have been analyzed in detail (e.g., Tegmark et al. 2004; Tempel et al. 2014).

Direct detections of the HI gas inside these structures in emission is more challenging and will require the sensitivity of upcoming radio telescopes like the Square Kilometer Array (SKA) to reach the required sensitivity (see Chapters 3 and 4; Takeuchi et al. 2014; Popping et al. 2015). However, faint galaxies that lie below the detection limit are instead more accesible to study with current radio observatories. Despite their relatively low HI content, these galaxies are more numerous than their high mass counterparts due to the shape of the HI mass function (e.g., Jones et al. 2018) and can therefore collectively encompass a large amount of HI gas.

Recently, the intensity mapping technique (Madau et al. 1997) has become a popular probe for faint emission beyond the capability of standard galaxy surveys, since it does not require the source of the emission to be fully resolved. This technique has been succesful in constraining the large-scale structure through HI 21 cm emission at $z \sim 0.8$ (Chang et al. 2010; Masui et al. 2013). In Takeuchi et al. (2014), a similar method to detect the emission from the IGM in filaments was proposed and further worked out in Chapter 3. Like intensity mapping, the idea proposed there is not to fully resolve the faint IGM in filaments, but instead to add together all the emission and get a single integrated detection per filament.

In this work, we use the same technique presented in Chapter 3, but instead switch focus from the IGM to the low-surface brightness galaxies within the filaments. We explore different methods to find filaments from galaxy surveys. Additionally, a comparison is made between the properties of filaments inferred from either optical and infrared galaxy surveys or their HI counterparts. Since the galaxies that are detectable or bright at optical/infrared wavelenghts can be different from those strong in HI 21 cm emission, the structures they trace are also not necesarrily all the same. We make use of a cosmological hydrodynamic simulation to realistically estimate the properties of both galaxies and the IGM within a volume large enough to contain many large-scale filaments. We then infer the locations of the filaments by creating mock galaxy catalogues and selecting galaxies in them based on the properties that can be detected using the surveys.

From the simulated filaments, predictions are then made for the upcoming HI surveys with the Apertif instrument on the Westerbork Synthesis Radio Telescope (WSRT; Oosterloo et al. 2009) for filaments at $z = 0.05$. The

large 8 deg^2 field of view of Apertif makes it possible to obtain deep integrations of large areas on the sky and will therefore open up the possibility for targetting multiple large-scale filaments within a survey. Furthermore, we perform estimates for the amount of HI gas that is hidden in galaxies fainter than the Apertif detection limit, assuming a 4σ detection threshold, but that could be probed by integrating along the filaments.

This chapter is built up as follows. In Section 5.2, we describe the simulation and introduce codes that can be used to infer filament spines from the positions of the galaxies. The Apertif medium deep survey area is then examined for the filaments this survey can find in Section 5.3. Section 5.4 describes the selections we make in the simulated galaxies, in order to infer filament spines based on optical and HI-based galaxy samples. The resulting properties of the filaments and their galaxies are then presented in Section 5.5. The chapter concludes in Section 5.6 with a discussion. For all the cosmological parameters used here, we refer to the Planck Collaboration et al. (2014) results.

5.2 Simulation

Given the lack of observations, simulations are required to make realistic estimates for the properties of large-scale filaments and the galaxies within them. In particular, the emission from the IGM is highly uncertain (see Chapter 4). In the following section, we describe which simulation was used here and how we find the large-scale filaments within it. We explore two methods to find filaments and make a comparison between them.

5.2.1 EAGLE

In order to obtain good statistics of the filaments, we require a simulation with a large volume that contains many filaments, as well as a simulation that takes into account all the relevant astrophysical processes. Therefore, we use the biggest simulation in the Evolution and Assembly of GaLaxies and their Environments (EAGLE) suite: Ref-L0100N1504 (Schaye et al. 2015; Crain et al. 2015; McAlpine et al. 2016). This box has a volume of 100 Mpc^3 with 1504^3 dark matter particles and the same amount of baryonic particles. The dark matter particles have masses of $9.70\times10^6\,\mathrm{M}_\odot$ and the gas particles $1.81\times10^6\,\mathrm{M}_\odot$ (The EAGLE team 2017). The $z=0$ snapshot of this box is placed on a grid of 512^3 cells through cloud-in-cell interpolation.

We then mask cells with overdensities above the virial limit and determine the HI fraction and 21 cm brightness temperature in the remaining cells through the algorithm presented in Chapter 3 and Chapter 4 of this thesis. This then gives us the HI content in the IGM, where we assume that it is affected by the ultraviolet (UV) background given by Puchwein et al. (2018).

From the publicly released EAGLE galaxy catalogue (McAlpine et al. 2016), we obtain the properties of the individual galaxies in the volume. This includes their spatial positions, as well as their star formation rates, stellar masses and their absolute magnitudes at specific wavelenghts. To make sure that the properties of each galaxy are based on at least a few particles of the simulation, we limit ourselves to galaxies with stellar masses greater than $M_\star \geq 10^7 M_\odot$ for this study. The resulting 142,343 galaxies considered here span 5 orders of magnitude in stellar mass. Galaxies of even lower mass are more numerous, but they cannot be resolved in this simulation and their HI masses would also be lower and would thus not add significantly to the total HI content inside a filament.

5.2.2 Bisous filament finder

Multiple methods to derive filamentary structures from simulations exist (e.g., Libeskind et al. 2017). However, where most codes require a density field to find structures, when dealing with observations they need to be able to trace filaments from the positions of galaxies alone. One of the codes that is able to do this is the Bisous filament finder (Tempel et al. 2014, 2016). This code determines the spines of filaments by statistically checking if galaxies are aligned. It does this by randomly connecting cyllinders around the galaxies of a certain length and radius using a marked point process. This method can find filaments of a particular scale and therefore can be applied particularly well to sparse samples of galaxies that are typically obtained in galaxy surveys. On the other hand, it also requires fixing multiple parameters before a run, which makes it relatively complex to use and it can be time consuming for large samples of galaxies.

5.2.3 Filament with DisPerSE

Another code that can easily be applied to observations is *DisPerSE* (Sousbie 2011; Sousbie et al. 2011). This code is not just limited to filaments and can also be used to find walls and voids within a simulation. The method

is based on discrete Morse theory that makes it possible to infer different structures from topological principles. It does this on any scale and therefore also traces the weak filaments inside voids. The structures it infers depend on their so called persistence value.

Persistence is a measure of how significant a structure stands out. The Poisson noise dominating the positions of galaxies typically have low persistence, whereas a large structure, such as a filament, would be measured with high persistence. The DisPerSE code therefore makes it possible to robustly find any structures in the data and it only requires a choice in the cut-off value of the persistence of the determined structures, making it very user friendly and fast to run. For the filament catalogues derived using DisPerSE here, we adopt a persistence value of 4σ above the noise.

5.2.4 Bisous vs DisPerSE

Given the very different methods used by both filament finding algorithms, it can be expected that the structures they find are also not the same. To test how well they work, we apply them both to a sample of galaxies in EAGLE with non-zero star formation rates and $M_\star \geq 10^8 M_\odot$.

In Fig. 5.1, a small cut-out of the HI 21 cm differential brightness temperature distribution in the simulation is given, where we show the filaments found by the Bisous code in light blue and the DisPerSE filaments as magenta lines. Overall, both codes trace most of the major structures well. The Bisous code tends to break the longer filaments up into smaller pieces, whereas DisPerSE keeps those together more. Both methods also infer filaments in positions where there visibly are none in the density field of the simulation. This is due to chance alignments of the galaxies that are interpreted as a real connection by the codes. Their integrated HI 21 cm signal would thus also be low. We therefore only consider filaments longer than 5 h^{-1}Mpc. Although the details in the filament spines from each code are different, they result in filaments of similar strenghts of IGM emission and can thus be considered equally appropriate for finding filaments from observations. Given that DisPerSE is faster to run, we use this code in most of the remainder of this work.

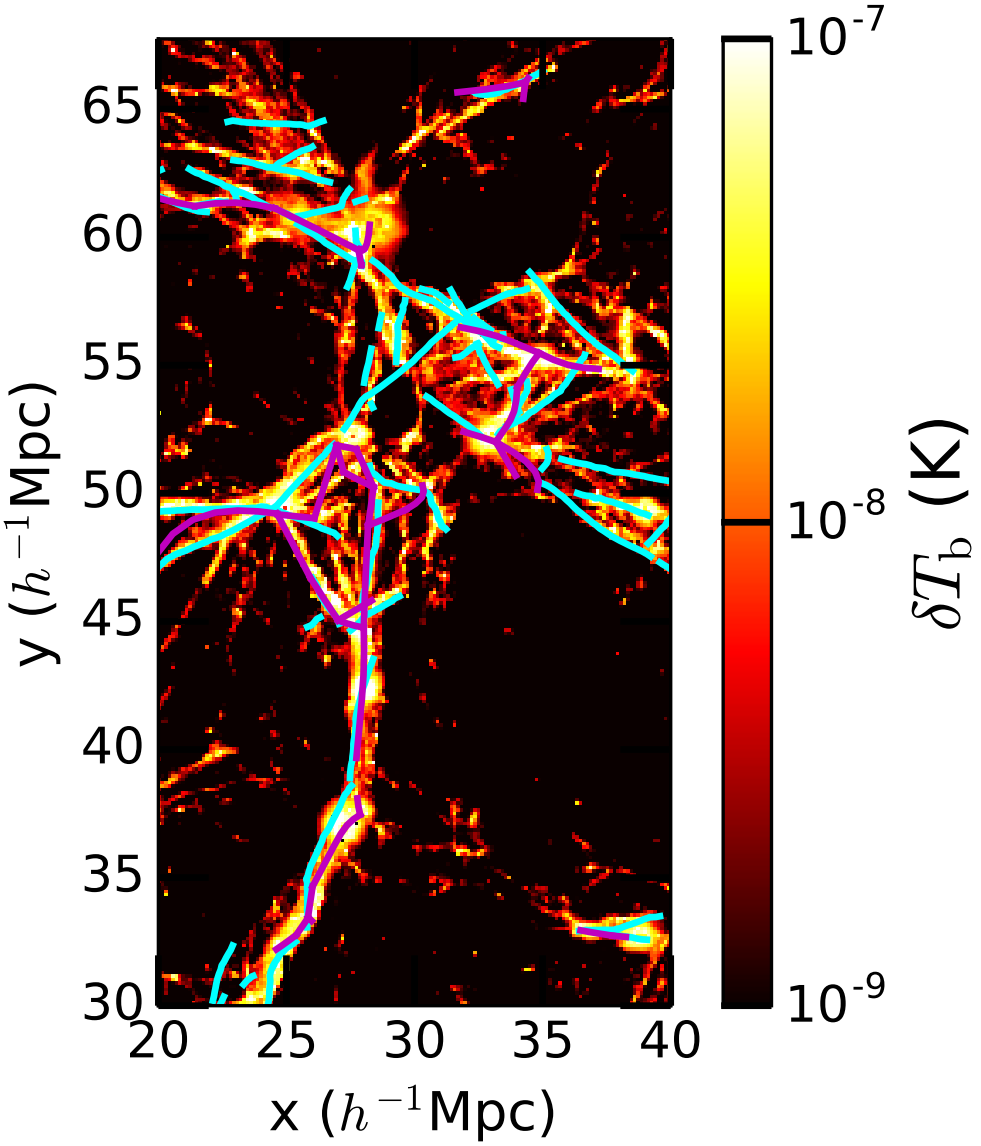

Figure 5.1: A slice of the HI 21 cm differential brightness temperature in the EAGLE simulation, assuming the Puchwein et al. (2018) UV background. Filaments are shown that have been inferred from a galaxy catalogue based on the star forming EAGLE galaxies with stellar masses $M_\star \geq 10^8 M_\odot$. The Bisous filaments are given by the light blue lines, whereas DisPerSE filaments are shown in magenta.

5.3 Filaments in the Apertif Medium-Deep survey

The upcoming medium deep survey[7] of Apertif will cover an area of 450 deg^2 with 84-120 hour integrations per pointing of 8 deg^2. We present some characteristic numbers of the telescope and the survey in Table 5.1. The sensitivity of the telescope is too low to detect the IGM in HI emission (see Chapter 3) and in Section 5.A of the Appendix, we show how spatial filtering by the Apertif point spread function further affects the diffuse emission from the IGM. Given the scope of this survey, Apertif will, however, be able to detect HI emission from many galaxies over a large area on the sky. This makes it an ideal survey to study the connection between the cosmic web and galaxies. Furthermore, the survey area will have overlap with multiple galaxy redshift surveys that have been performed on the northern sky before and, therefore, it is already possible to infer the positions of filaments that lie within the survey area. Apertif will find more galaxies than an optical survey, such as SDSS. This can help improve the reliability of inferred filaments. A larger sample of galaxies would also help to find more filaments and, as such, trace the cosmic web in more detail. Nevertheless, the currently available data is expected to be enough to identify the location of the major structures.

To give the reader a feeling for the sheer number of filaments that can be traced with the medium deep survey, we plot the spines of several large filaments on top of the red shaded survey area in Fig. 5.2. The blue lines show filament spines going out to $z = 0.1$ and with lenghts $l \geq 10\ h^{-1}$Mpc inferred through the positions of SDSS galaxies. These spines were found using the Bisous code and are publically available as the filament catalogue by Tempel et al. (2014). Aditionally, we show Bisous filament spines determined using galaxies detected in 2MRS as green lines and from a combined sample of 2MRS and the 6-degree Field (6dF) Galaxy Redshift Survey (Jones et al. 2004, 2009) as black lines. Even though the galaxies of 2MRS are also used by the sample of galaxies for the black spines, the additional information from the 6dF galaxies makes it possible to find more filaments and also slightly affects the exact geometry of each filament. This can be most clearly seen in the right panel of Fig. 5.2, where some of the black lines lie close to the green ones, but they are slightly different.

[7] http://www.astron.nl/radio-observatory/apertif-surveys

Table 5.1: Properties of the Apertif instrument on the WSRT and its medium deep survey.

Parameter	Value
Number of dishes	12
Collecting area	5890 m^2
System temperature	70 K
Aperture efficiency	0.7
Field of View	8 deg^2
Beamsize	$15'' \times 15''/\sin(\delta)$
Frequency resolution	36.6 kHz
Survey area	300 deg^2
Integration time per pointing	84-120 h
Column density sensitivity (4σ)	$1{\times}10^{20}\,cm^{-2}$

Also, the most dense sample of galaxies comes from SDSS and that thus also results in the largest amount of filaments that can be found from it. Since Apertif will be more sensitive than SDSS, it will clearly find even more filaments and make it possible to do a larger statistical study of the galaxies and their environment. How well a catalogue of filaments from an optical survey, such as SDSS, compares to one that can be inferred from galaxies detected through HI emission by Apertif will be examined further in Section 5.5.

5.4 Tracing filaments with different galaxy surveys

Since large-scale filaments provide the dense environments in which most of the galaxies form, following the filaments is a good way to find emission from faint galaxies that fall below the detection limit. In order to find the filaments inside an HI survey, it is possible to either use the positions of galaxies detected in the survey itself, or those from pre-existing galaxy

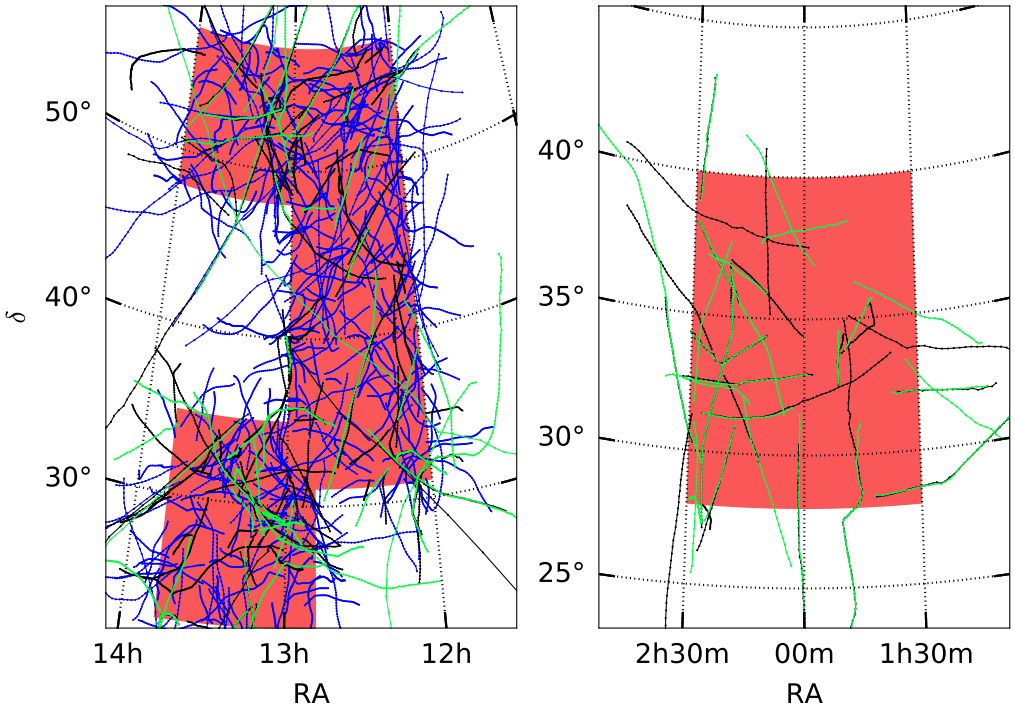

Figure 5.2: Bisous filaments with $l \geq 10\ h^{-1}$Mpc and $z \leq 0.1$ in the medium deep survey area of Apertif denoted by the shaded areas in red. The blue lines denote the filament spines from SDSS, the green ones the spines from 2MRS and the black spines are from the combined sample of 2MRS and 6dF galaxies. The two plots show the target fields on opposite sides of the Galactic plane.

redshift surveys. In this section, we explore the properties of the filaments that are inferred from a galaxy sample in the EAGLE simulation based on the sensitivity of Apertif and a sample based on the sensitivity of SDSS. In both cases, we apply the DisPerSE filament finder with a persistence threshold of 4σ and also determine the HI content in both the faint galaxies below the Apertif detection threshold and the HI content in the IGM around the filament spine. This will be helpful to estimate how much HI mass can still be found inside the filaments by integrating all the faint emission.

5.4.1 SDSS-based galaxy catalog from EAGLE

For the EAGLE simulation, the brightness of the galaxies with stellar masses above $10^{8.26}\mathrm{M}_{\odot}$ has been calculated in multiple bands and is available in the public database (Trayford et al. 2015; McAlpine et al. 2016). For a subsample of this, galaxies that have more than 250 dust particles, the fluxes have been recalculated to include dust attenuation (Camps et al. 2018). Since the apparent brightness depends on the geometry of the dust inside the galaxy and, consequently, the angle at which the galaxy is observed, an assumption for the viewing orientation needs to be made. In this case, we adopt the random viewing orientation given in the catalogue for the dust-corrected fluxes.

The absolute magnitudes can be converted to apparent magnitudes at a given redshift through the distance modulus

$$m_z = M + 5 \cdot \log\left(\frac{d_\mathrm{c}(z)(1+z)}{10\,\mathrm{pc}}\right), \tag{5.1}$$

where $d_\mathrm{c}(z)$ is the comoving distance to redshift z and M is the absolute magnitude given in the catalogue. The r-band magnitudes as a function of stellar mass are shown in Fig. 5.3.

The spectroscopic sample of SDSS was limited in r-band magnitude by $m_\mathrm{r} \leq 17.77$ (Strauss et al. 2002) and we apply the same limit to the sample of EAGLE galaxies. This results in a total of 6,083 galaxies that SDSS would be able to detect within the volume of the simulation. From this sample, we infer a total of 262 filament spines longer than 5 h^{-1}Mpc.

5.4.2 Apertif-based galaxy catalogue from EAGLE

In a similar manner, we create a catalogue of filaments traced by galaxies that can be detected by Apertif. However, in this case the selection becomes more complicated because the EAGLE simulation itself does not provide information on the HI content of the galaxies, only the total gas content. A radio telescope, such as Apertif, is sensitive to surface brightness, or HI column density. For high-mass galaxies, the size of the HI disk can be larger than the size of the synthesized beam. In this case, the surface brightness distribution of the galaxy becomes important for a detection of its HI gas, since the telescope can then resolve the structures inside the disk. For example, spiral arm features can result in significantly higher surface

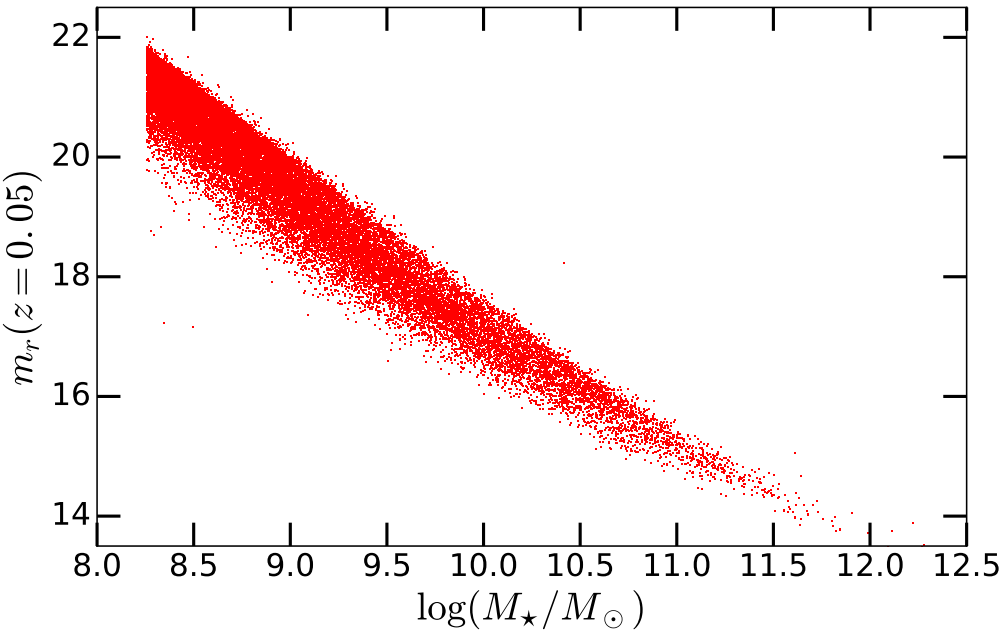

Figure 5.3: The r-band apparent magnitude at $z = 0.05$ of the galaxies in the EAGLE simulation as a function of their stellar mass.

brightness in certain areas of the galactic disk. Therefore, we assume that all galaxies larger than the size of the synthesized beam (corresponding to ~16 kpc at z = 0.05) can be detected. Using the observationally derived HI mass-size relation from Wang et al. (2016), this limit would correspond to galaxies with an HI mass of $\log M_{\rm HI} \sim 8.92$. Galaxies that are smaller than the size of the beam, on the other hand, can be treated as point sources. In that case, the column density of the galaxy is given by

$$N_{\rm HI}^{\rm gal} \approx \frac{M_{\rm HI}}{D_{\rm res}^2}, \tag{5.2}$$

where $D_{\rm res}$ is the physical size corresponding to the angular size of the resolution of the telescope. By inverting this relation, the corresponding HI mass limit for galaxies that can be detected by Apertif becomes $M_{\rm HI} \geq 10^{8.3}\,{\rm M}_\odot$ for 4σ and $M_{\rm HI} \geq 10^{7.7}\,{\rm M}_\odot$ for 1σ.

To select galaxies based on the sensitivity of Apertif, we need to derive the HI masses of the galaxies in the EAGLE simulation. For galaxies with

$M_\star \geq 10^9\,\mathrm{M}_\odot$, we adopt HI masses calculated by Marasco et al. (2016) that are based on the methods described in Bahé et al. (2016) and Crain et al. (2017). We take the HI masses derived within a sphere with a radius of 150 kpc around the galaxies. For some of these galaxies, the derived HI mass falls below the mass of a single particle in the simulation. For these cases we assume that these galaxies do not contain any HI mass, since any mass lower than that cannot be resolved.

Crain et al. (2017) found that, for galaxies with stellar masses below $10^9 M_\odot$, EAGLE poorly reproduces the volumetric HI mass function and, in general, the stellar mass to HI mass relation is underestimated. This is a consequence of the limited resolution of this simulation and is a trade-off we make to obtain a large enough volume to find as many filaments as possible. For the higher-stellar mass galaxies, the derived properties are reasonable.

Therefore, for the lower-stellar mass end, we assume that they are all late-type galaxies and adopt the double power-law fit to the observed HI mass-stellar mass relation from (Calette et al. 2018):

$$M_{\mathrm{HI}} = \frac{M_\star C}{\left(\frac{M_\star}{M_\star^{\mathrm{tr}}}\right)^a + \left(\frac{M_\star}{M_\star^{\mathrm{tr}}}\right)^b}. \tag{5.3}$$

Here C, a and b are constants and $M_\star^{\mathrm{tr}}$ is the mass at which the function transitions to the second power-law. The best-fit values for the constants are: $C = 0.98 \pm 0.06$, $a = 0.21 \pm 0.04$, $b = 0.67 \pm 0.03$, $\log M_\star^{\mathrm{tr}} = 9.24 \pm 0.04$. This relation has a natural scatter of 0.52 dex. We mimic this variation by adding normally distributed random numbers to the logarithm of the HI mass of these low-end stellar mass galaxies. This results in the distribution of HI mass vs stellar mass shown in Fig. 5.4. There is a discrepancy of ∼0.2 dex between the distribution of HI masses at stellar masses below $10^9 M_\odot$ and those above it. This follows from the poor reproduction of the HI mass function by this simulation, as discussed above (Marasco et al. 2016; Crain et al. 2017). When using HI masses determined by halo membership for the high-mass end, the discrepancy increases to ~ 0.5 dex.

To determine the filaments that can be found with galaxies detected by Apertif, we adopt the 4σ limit in HI mass derived above and exclude all galaxies below this limit, resulting in a sample of 36,855 galaxies and 574

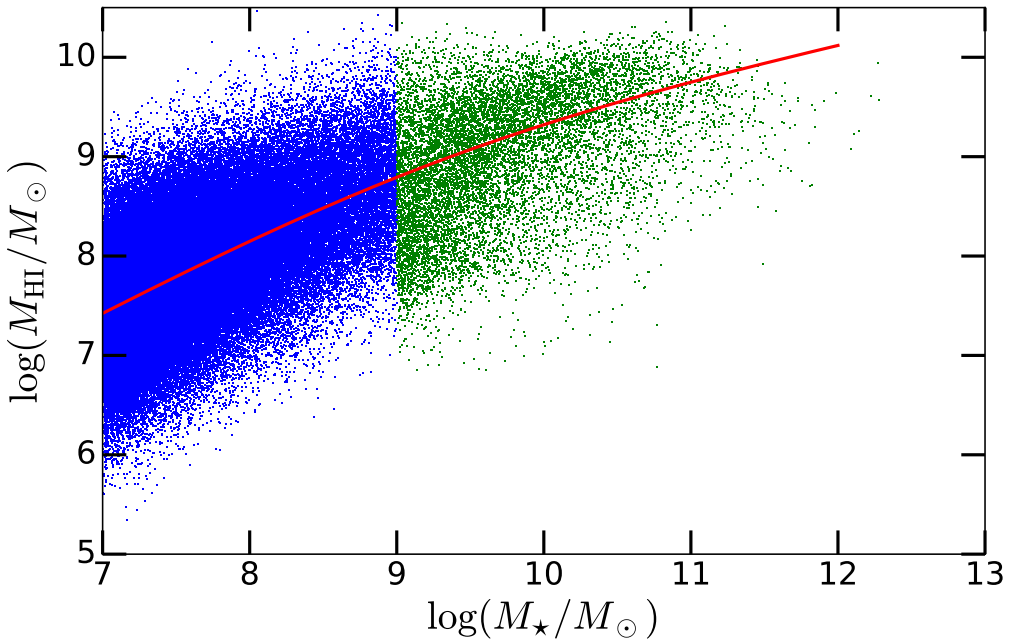

Figure 5.4: HI mass - stellar mass relation from the galaxies in the EAGLE simulation. The green dots show the galaxies whose HI mass has been determined by Crain et al. (2016). The red line shows the observationally determined relation given by Equation 5.3. The blue dots then show the HI mass from galaxies at the lower stellar mass end which are randomly distributed around the red line with a scatter of 0.52 dex.

filaments longer than 5 h^{-1}Mpc that can be inferred from it. We will refer to this sample of filaments as Apertif filaments and the sample described in Section 5.4.1 as SDSS filaments.

5.5 Results and Discusion

Using the two filament catalogues from Section 5.4, we make a comparison of the properties of the galaxies around the filaments and of the average properties per filament. Finally, we determine the HI mass in galaxies below the detection limit of Apertif to estimate how much HI mass can still be detected with the same instrument by integrating along the filaments.

5.5.1 Properties of filament galaxies

Since optical telescopes are sensitive to different galaxy properties than radio telescopes, they can in principle also trace different regions of the large-scale structure. Here, we check if this also means that the cosmic web they trace as a whole has different properties by selecting all the galaxies in the EAGLE simulation within a radius of $0.5h^{-1}$Mpc from any of the filament spines. The sample of SDSS filaments contains 17,932 galaxies in the simulation, whereas the Apertif filaments contain a total of 21,351 around the spines longer than 5 h^{-1}Mpc. This radius results in the probing of a volume of 1954 and 3334 $(h^{-1}\text{Mpc})^3$ for SDSS and Apertif filaments, respectively. The distributions of the properties of these galaxies can be found in Fig. 5.5.

As can be seen, the filaments from both samples as a whole trace roughly the same kind of galaxies. The distribution of stellar mass increases towards lower masses, as expected. Interestingly, the distribution of HI mass decreases from $10^8 M_\odot$ to lower mass. One possible explanation could be that the filaments are feeding the HI content of the galaxies, preventing lower HI mass galaxies from forming there. However, the limited resolution in the simulation does not allow us to analyze this in more detail.

Most galaxies inside the simulation have zero star formation rate, or very low star formation rate set to zero in the simulation, which is shown as the sharp peak at the 0-1 $M_\odot$/yr bin on the left side of the plot. However, the filaments in the simulation do still contain hundreds of star forming galaxies, where Apertif would find a bit more because it can trace more filaments. The color of the galaxies found by looking around Apertif filaments also tends to be a bit more blue, although the difference in the distribution is small. Apertif filaments thus seem to be able to trace slightly younger galaxies, as expected.

5.5.2 Average properties of filaments

While the difference in the properties of the complete sample of galaxies around the two samples of filaments is negligible, Apertif and SDSS are able to find different filaments. Therefore, we also show the properties of the filaments themselves in Fig 5.6.

The filaments traced by galaxies that SDSS can detect might be longer. This is a consequence of the more detailed information on the structure in the

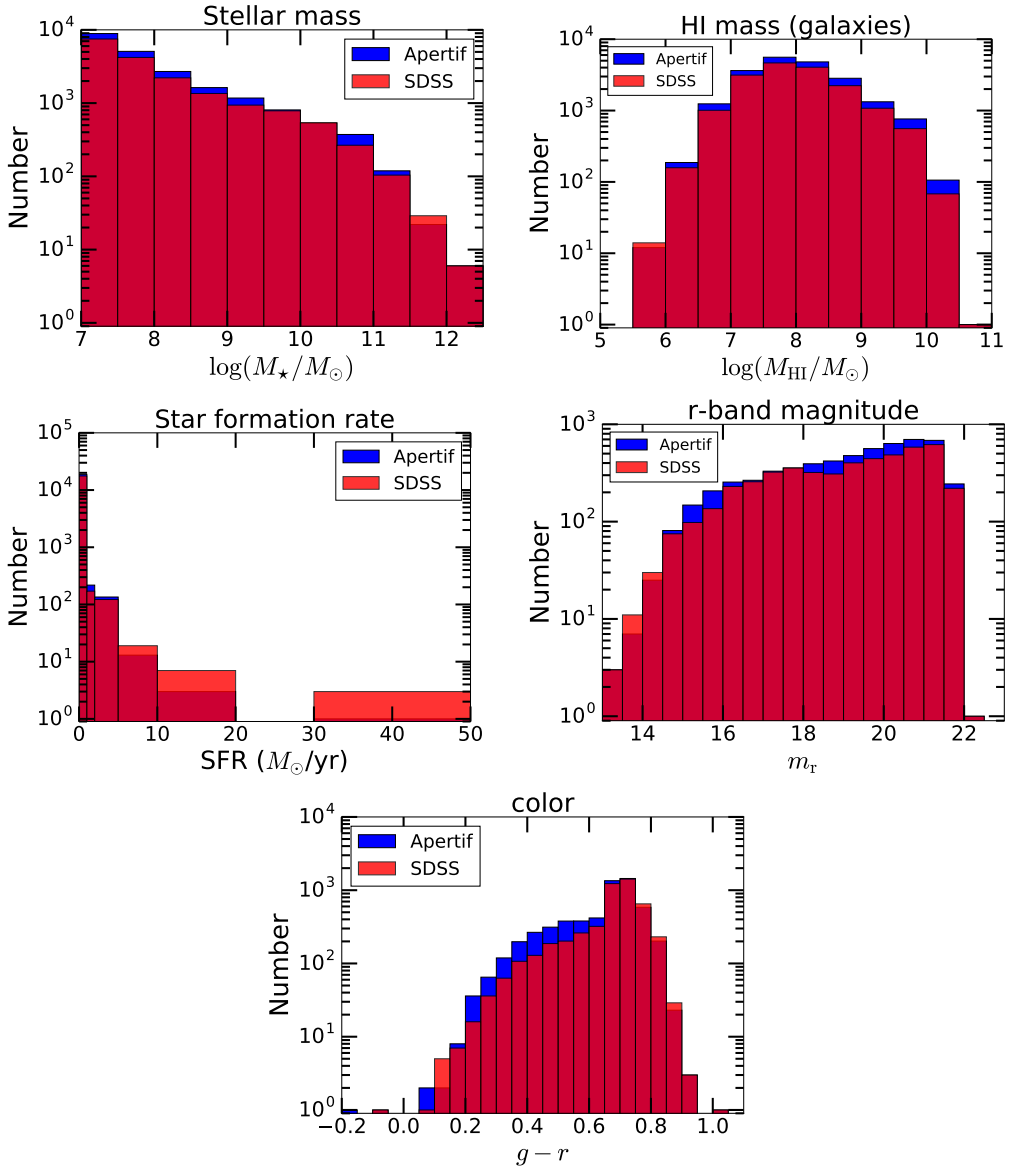

Figure 5.5: Distributions of the properties of galaxies traced by the filaments based on the Apertif sensitivity (blue) and the SDSS sensitivity (red). The stellar mass of all the galaxies within 0.5 h^{-1}Mpc of the filament spines is shown top left. The top right plot shows their HI masses. The middle row shows the distribution of star formation rates and r-band magnitudes for the galaxies and the bottom plot displays the distribution of their g-r colors.

larger sample of galaxies that define the Apertif filaments. Since the Apertif sample contains more galaxies in the branches of the main filaments, the filament finder tends to break up the longer filaments into slightly shorter pieces. These might also be more recently formed filaments that contain younger galaxies, whereas the bigger structures are likely to be older, containing older and thus more red galaxies. A similar effect to that of the different filament lengths can also be seen when looking at the mean overdensity inside the filaments, where the SDSS filaments are able to slightly better trace the very high overdensities $\delta > 10$. However, when considering filaments with overdensities $0 > \delta \leq 10$, Apertif is able to find significantly more.

A small number of filaments in both samples are misaligned with the density field, or trace very weak filaments. Apertif finds a few more of these because its filaments are inferred from more galaxies or because the galaxies and filaments it traces can be younger. This effect can be most clearly seen in the distribution of the mean HI 21 cm brightness temperature signal, where Apertif finds more filaments with low signal, but overall it also manages to find more strong filaments than SDSS would. Therefore, when one is interested in detecting the emission from the IGM, it is best to infer filaments from HI selected galaxies. This will mainly be useful for SKA.

The difference between the distribution of color of the galaxies found in the filaments in Section 5.5.1 is more pronounced in the mean color of the galaxies per filament. The Apertif filaments clearly find more blue, and thus younger, galaxies within them. Do note, however, that most of the redder galaxies found by SDSS filaments are also encompassed in the sample of Apertif filaments, so the difference is mainly a consequence of the extra filaments that an Apertif-based sample of galaxies is able to trace.

5.5.3 HI content of filaments

The HI content of the filaments can vary significantly from filament to filament. However, on average there is hardly any difference between the HI contents found in filaments traced by SDSS and those traced by Apertif, as far as this limited study can tell. Surveys that are sensitive to only the brighter galaxies might show stronger differences than the ones considered here. With the Apertif medium deep survey it will be possible to detect a total HI mass in the galaxies per filament of $\log(M_{\rm HI}^{\rm Gal}/M_\odot) = 10.3 \pm 0.5$ with

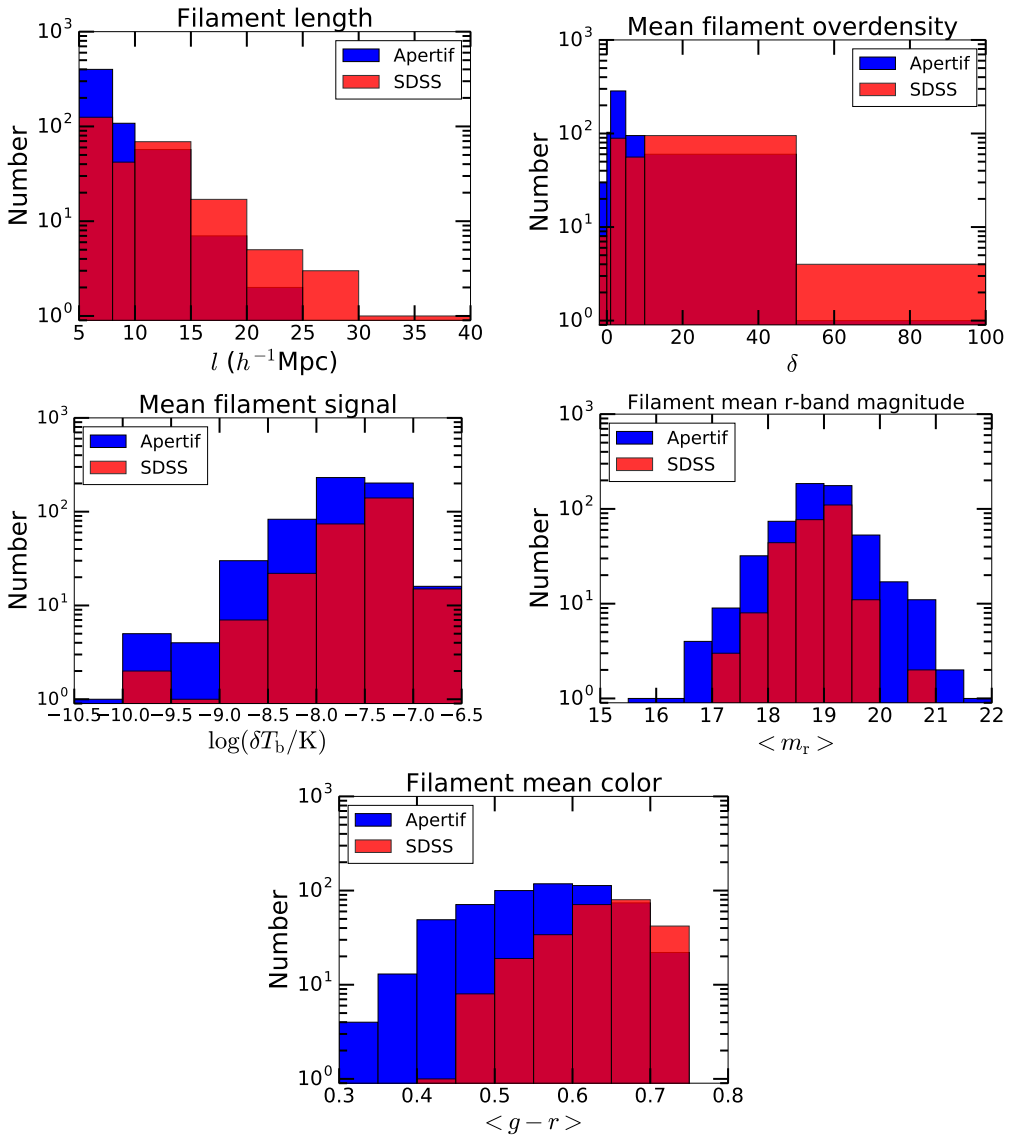

Figure 5.6: Distributions of the average properties of the filaments inferred from the sample of galaxies from Apertif (blue) and those from SDSS (red). The length of the filaments and the mean overdensities of the filaments are shown in the top row. The second row gives the distribution of the mean HI 21 cm signal of the filaments on the left and the mean r-band magnitude per filament on the right. The bottom plot gives the mean g-r color.

4σ or more significance for filaments traced by Apertif itself. This number becomes $\log(M_{\rm HI}^{\rm Gal}/M_\odot) = 10.6 \pm 0.4$ for filaments inferred from SDSS. As was seen before, the difference between both filament samples is small, but since the smaller sample from SDSS is more focused on the major structures of the cosmic web, the mean is also slightly larger. The distribution of the total HI mass in galaxies per filament is shown in the left plot of Fig. 5.7.

Faint emission might not be detected by Apertif directly, but by tracing a filament and integrating all the emission around it, it will still be possible to detect a significant amount of hidden HI gas. The galaxies that Apertif will be able to observe with a significance of 4σ to 1σ will contain an average HI mass per filament of $\log(M_{\rm HI}^{\rm Gal}/M_\odot) = 9.2 \pm 0.4$ in Apertif filaments and $\log(M_{\rm HI}^{\rm Gal}/M_\odot) = 9.5 \pm 0.4$ in the filaments from SDSS. If it is possible to go even deeper, there will still be HI contents of $\log(M_{\rm HI}^{\rm Gal}/M_\odot) = 8.6 \pm 0.4$ (Apertif filaments) and $\log(M_{\rm HI}^{\rm Gal}/M_\odot) = 9.0 \pm 0.5$ (SDSS filaments) inside the galaxies traced per filament below the 1σ detection threshold for individual galaxies with Apertif.

For both samples, the IGM traced by the filaments contains an average HI mass of $\log(M_{\rm HI}^{\rm IGM}/M_\odot) = 8.6 \pm 0.5$, as shown in the right panel of Fig. 5.7. Since this is lower than the HI mass from galaxies that can be directly detected by Apertif, it would not be able to distinguish between the integrated emission from faint galaxies and that of the IGM. However, a more sensitive telescope, such as the SKA, would be able to find enough faint galaxies to bring their contribution down to below that of the IGM.

5.6 Conclusion

The large-scale structure of the Universe plays an important role in the formation and evolution of galaxies. In this work, we used various methods to study what kind of information can be obtained on the HI content of cosmic web filaments. The 100 $\rm Mpc^3$ EAGLE simulation was used to obtain realistic properties of filaments and their IGM, and we checked multiple ways of inferring the location of filaments from the distributions of galaxies that are representative of how this can be applied to observations with the Apertif instrument at $z = 0.05$.

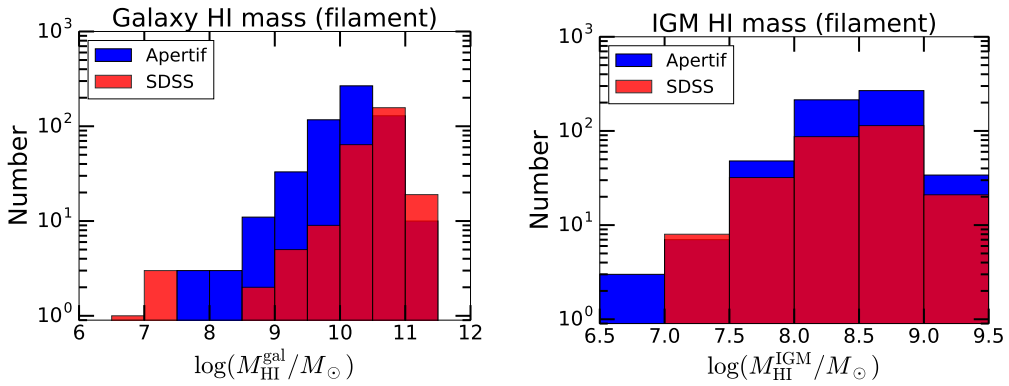

Figure 5.7: Distributions of the average HI properties of the filaments inferred from the sample of galaxies from Apertif in blue and those from SDSS in red. The left panel gives the total HI content per filament of all its galaxies within a distance of $0.5h^{-1}$Mpc from the spine. On the right, it shows the distribution of the total IGM HI content of the filaments.

By applying the Bisous filament finder and the DisPerSE code to the same sample of galaxies, we find that both codes manage to trace most of the major structures in the simulation in a similar manner.

We then specifically focus on the Apertif medium deep survey. Within its proposed survey area, it is already possible to find hundreds of filaments based on the sample of SDSS galaxies alone. Apertif itself will be able to detect more galaxies and thus more filaments.

We then applied the sensitivity of SDSS and Apertif to the galaxies in the simulation to check for a difference in the properties of the filaments that can be inferred with an optical/infrared survey versus an HI survey using the HI 21 cm line. With these galaxy samples, we can infer ~300 filaments with SDSS and almost twice as many using Apertif. The properties of the galaxies inside the filaments follow roughly the same distribution between both samples. The SDSS filaments find most of the major filamentary structures in the simulation, but as a whole, the properties of the filaments that can be found are similar to those that Apertif would be able to trace from the galaxies it can detect. Apertif filaments can trace a population of slightly more blue, or younger galaxies.

Within each filament, we find that there will be a significant amount of HI

gas hiding below the detection limit of individual galaxies with the Apertif medium deep survey. The faint galaxies between the 4σ and 1σ detection thresholds of Apertif together contain an HI mass of $\sim 10^9 M_\odot$ per filament, which is more than the HI gas that can be found in their IGM. By tracing the filaments in the survey and integrating all the HI 21 cm emission around their spines, the Apertif medium deep survey will thus be able to detect a large amount of HI gas in the faint galaxies, even if it cannot detect the galaxies separately.

This work can also be extended to higher redshift (e.g., z = 2-3), where the star formation rate density of the Universe peaks. Since filaments can provide galaxies with the fuel for star formation, it can be expected that the difference in properties of filaments traced by infrared galaxies and HI galaxies will be larger. These estimates can then be applied to existing surveys that trace Lyman alpha emission or absorption to see what kind of filaments can be traced from them. We plan to apply the methods described here to studies using the Lyman alpha forrest to examine their ability to trace the hydrogen content in the IGM and faint galaxies.

Bibliography

Aihara H., et al., 2011, ApJS, 193, 29

Bahé Y. M., et al., 2016, MNRAS, 456, 1115

Calette A. R., Avila-Reese V., Rodríguez-Puebla A., Hernández-Toledo H., Papastergis E., 2018, preprint, (`arXiv:1803.07692`)

Camps P., et al., 2018, ApJS, 234, 20

Chang T.-C., Pen U.-L., Bandura K., Peterson J. B., 2010, Nature, 466, 463

Colless M., 1999, in Efstathiou G., et al. eds, Large-Scale Structure in the Universe. p. 105

Crain R. A., et al., 2015, MNRAS, 450, 1937

Crain R. A., et al., 2017, MNRAS, 464, 4204

Huchra J. P., et al., 2012, ApJS, 199, 26

Jones D. H., et al., 2004, MNRAS, 355, 747

Jones D. H., et al., 2009, MNRAS, 399, 683

Jones M. G., Haynes M. P., Giovanelli R., Moorman C., 2018, MNRAS, 477, 2

Libeskind N. I., et al., 2017, preprint, (arXiv:1705.03021)

Madau P., Meiksin A., Rees M. J., 1997, ApJ, 475, 429

Marasco A., Crain R. A., Schaye J., Bahé Y. M., van der Hulst T., Theuns T., Bower R. G., 2016, MNRAS, 461, 2630

Masui K. W., et al., 2013, ApJ, 763, L20

McAlpine S., et al., 2016, Astronomy and Computing, 15, 72

McMullin J. P., Waters B., Schiebel D., Young W., Golap K., 2007, in Shaw R. A., Hill F., Bell D. J., eds, Astronomical Society of the Pacific Conference Series Vol. 376, Astronomical Data Analysis Software and Systems XVI. p. 127

Oosterloo T., Verheijen M. A. W., van Cappellen W., Bakker L., Heald G., Ivashina M., 2009, in Wide Field Astronomy & Technology for the Square Kilometre Array. p. 70 (arXiv:0912.0093)

Planck Collaboration et al., 2014, A&A, 571, A1

Popping A., Meyer M., Staveley-Smith L., Obreschkow D., Jozsa G., Pisano D. J., 2015, Advancing Astrophysics with the Square Kilometre Array (AASKA14), p. 132

Puchwein E., Haardt F., Haehnelt M. G., Madau P., 2018, preprint, (arXiv:1801.04931)

Schaye J., et al., 2015, MNRAS, 446, 521

Sousbie T., 2011, MNRAS, 414, 350

Sousbie T., Pichon C., Kawahara H., 2011, MNRAS, 414, 384

Strauss M. A., et al., 2002, AJ, 124, 1810

Takeuchi Y., Zaroubi S., Sugiyama N., 2014, MNRAS, 444, 2236

Tegmark M., et al., 2004, ApJ, 606, 702

Tempel E., Stoica R. S., Martínez V. J., Liivamägi L. J., Castellan G., Saar E., 2014, MNRAS, 438, 3465

Tempel E., Stoica R. S., Kipper R., Saar E., 2016, Astronomy and Computing, 16, 17

The EAGLE team 2017, preprint, (arXiv:1706.09899)

Trayford J. W., et al., 2015, MNRAS, 452, 2879

Wang J., Koribalski B. S., Serra P., van der Hulst T., Roychowdhury S., Kamphuis P., Chengalur J. N., 2016, MNRAS, 460, 2143

York D. G., et al., 2000, AJ, 120, 1579

Appendix 5.A Spatial filtering of IGM Emission with Apertif

Although point sources can be detected by the sensitivity of the full array for a radio interferometer, the sparse sampling of the u,v-plane by a telescope as Apertif causes some spatial filtering of diffuse emission. The main loss in signal would occur on diffuse structures with scales larger than the scale corresponding to the shortest baseline of the array. It therefore affects both emission from the IGM and galaxies that cover an area on the sky larger than the primary beam. The farther away the source, the smaller it becomes on the sky and thus the smaller will be the signal loss.

To study this effect, we created dirty images of three of the filaments in the simulation by convolving them with the point spread function (PSF) of the WSRT, where we project the images to multiple redshifts ($z = 0.02$ and 0.05). We then clean them with the *deconvolve* task in the Common Astronomy Software Applications package (CASA; McMullin et al. 2007) using the Hogbom algorithm with a gain of 0.7 and 30,000 iterations. In the top row of Fig. 5.8, the non-convolved images of the filaments are given, whereas the bottom row shows the results after convolution and cleaning. By integrating all the emission in between the black lines and dividing the cleaned images by the value obtained in the original images, we find that

the signal is decreased by a factor of ∼3-4 and ∼2 for $z = 0.02$ and 0.05, respectively.

We note that the sidelobes in the Apertif point spread function cause the bright spots in the images to completely dominate the fainter emission. Therefore, even if there is some IGM emission just below the detection threshold, it would be dominated completely by the brighter galaxies that reside within the filaments. However, the resolution of the simulation is limited and, therefore, some of the large structures in these images could in reality be built up of smaller clumps of gas that cannot be resolved here. We also performed the same calculation on a filament found in the higher resolution 25 Mpc^3 simulation box from the EAGLE suite. This filament is shown in the most right column of Fig. 5.8 and in this case, the signal loss at $z = 0.02$ decreases to a factor of ∼2. The exact effect of the spatial filtering depends on the geometry of the diffuse emission, but clearly for the larger scales in the IGM it cannot be ignored. With a telescope with more and shorter baselines, the effect will be smaller, as was shown in Chapter 4.

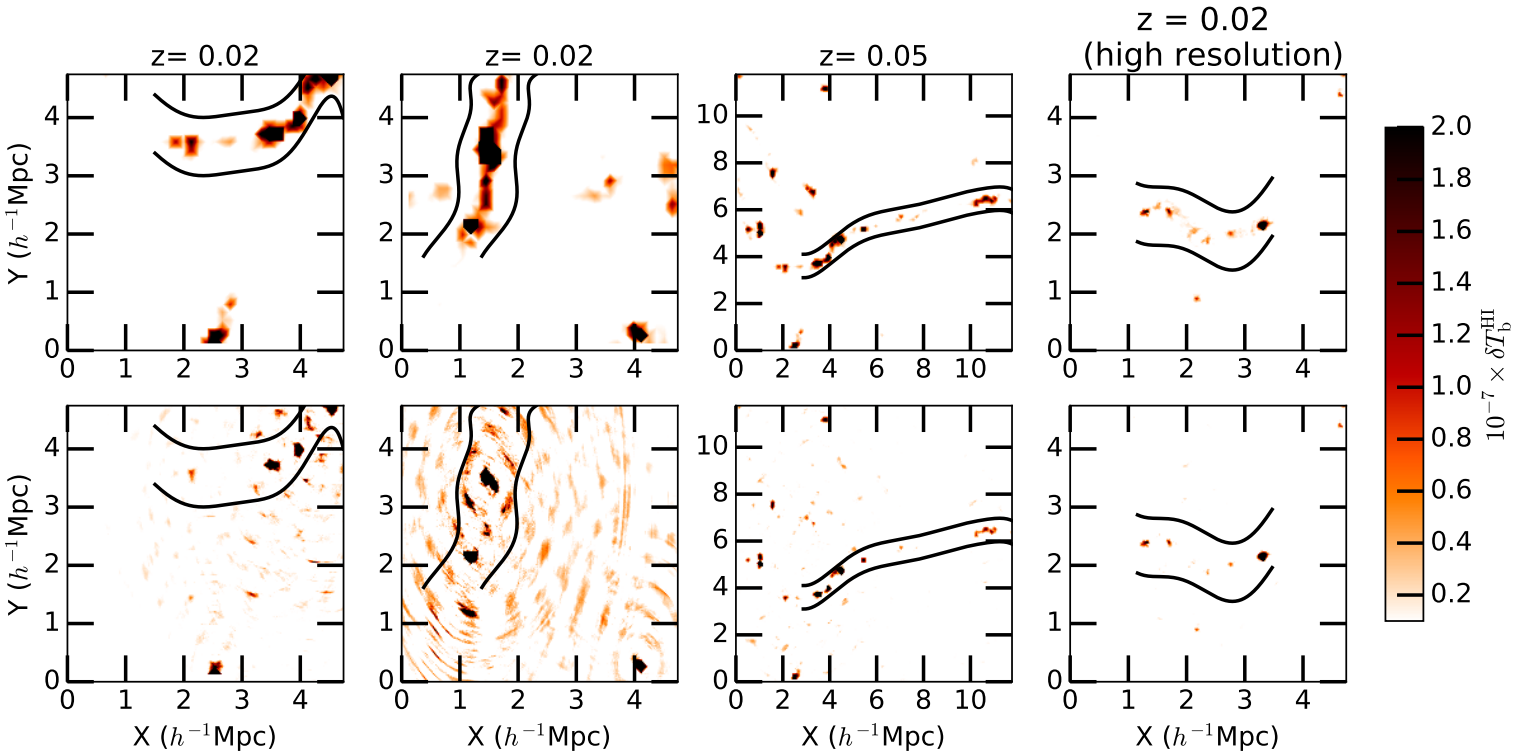

Figure 5.8: Deconvolution of simulated filaments. The top row shows the images directly from the simulation. The bottom row shows the signal that is recovered after the images have been convolved with the WSRT beam and after cleaning. The titles above the figures denotes the redshift to which the simulation was rescaled. The final column shows a filament extracted from the 25 Mpc^3 EAGLE simulation, which has higher resolution. In all images, the black lines highlight an area with a width of 1 h^{-1}Mpc around the interpolated spine of the filament in order to help guide the eye.